Preferential excitation of a single nanomagnet using magnetoelastic coupling

W. G. Yang,* M. Jaris,* C. Berk, and H. Schmidt†
School of Engineering, University of California Santa Cruz, 1156 High Street, Santa Cruz, California 95064, USA

(Received 26 December 2018; revised manuscript received 25 February 2019; published 29 March 2019)

We report preferential excitation and detection of the precessional spin dynamics of individual nanomagnets via magnetoelastic (MEL) resonance excitation. Surface acoustic waves (SAWs) are generated via the ultrafast optical excitation of a nonmagnetic grating (Al bars) with lithographically defined acoustic eigenmodes. We show that the precessional spin dynamics in two identical, elliptical nanomagnets with orthogonal orientations can be selectively excited by the SAWs via control of the applied magnetic field. Furthermore, we observe that both the amplitude and damping of the magnetoelastically induced precession depend on the relative orientation of the SAW with respect to the nanomagnets. Using magnetomechanical simulations, we show that the acoustic excitation is most efficient when the spatial distributions of the natural and SAW-driven magnetic resonances overlap. These findings reveal a direct connection between the geometry and MEL excitation efficiency and have implications for the rational design of nanoscale magnetomechanical devices.

DOI: 10.1103/PhysRevB.99.104434

I. INTRODUCTION

Nanostructured magnetic devices have long been identified as leading candidates for next-generation data storage [1–4]. Thanks to rapid advances in nanotechnology, more sophisticated nanomagnetic architectures are widely available, e.g., magnetic tunnel junctions, and have been intensely studied for their potential role in a variety of applications ranging from neuromorphic computing to microwave signal generation [5–8]. Because the operation characteristics of magnetic technologies intrinsically depend on their dynamic magnetic properties, a variety of techniques [9–12] have been developed to excite and measure the ultrafast spin dynamics of magnetic nanostructures.

One method of exciting ferromagnetic resonance that has become increasingly popular uses radio-frequency acoustic pulses, known as surface acoustic waves (SAWs), to resonantly excite spin dynamics via the magnetoelastic effect (MEL), also known as the inverse magnetostrictive effect [13–17]. The acoustic pulses periodically deform the magnetic sample in time and space, which in turn generates an internal MEL field that oscillates at the SAW frequency. However, only a few studies have investigated the transient response of single nanomagnets driven by SAWs [17,18], although such studies are crucial to the development of nanoscale magnetomechanical devices because they reveal the intrinsic magnetic properties that underpin the dynamic MEL interaction [8,17,19].

Recently, we introduced an all-optical technique that utilizes nonlocally generated SAWs to athermally drive spin dynamics in a remote, single nanomagnet [17]. Using this method, we reported time-resolved measurements of the SAW driven magnetization precession of a single magnetic nanostructure and showed that this technique can be used to directly determine the intrinsic Gilbert damping of the nanomagnet [17]. In this paper, we demonstrate that SAWs can be used to selectively excite spin dynamics in two identical, elliptical nanomagnets with orthogonal orientations. We observe the amplitude and damping rate of the MEL-driven precession depending on the direction of the SAW and sample geometry. The direct connection between the nanomagnet geometry and the characteristics of the MEL excitation has direct implications for the rational design of magnetoelastically controlled nanostructures.

II. EXPERIMENTS

In order to study the preferential excitation of single nanomagnets using SAWs, two identical elliptical Ni nanomagnets ($316 \times 160 \times 30\,\mathrm{nm}^3$) with orthogonal orientations were defined between two sets of identical, nonmagnetic aluminum (Al) bars [Fig. 1(a)] on a (100) Si substrate capped by a 110-nm-thick hafnium oxide antireflection coating [20,21] utilizing multilevel electron-beam lithography, electron-beam evaporation, and liftoff processes [17]. The Al bars (width = 220 nm, thickness = 30 nm) were fabricated with a pitch ($p = 410\,\mathrm{nm}$), corresponding to a SAW frequency ($f_{\mathrm{SAW}} = 7.8\,\mathrm{GHz}$) that is determined by the relation $f_{\mathrm{SAW}} = v_s/p$, where v_s is the speed of sound along the sample surface. To excite SAWs, the Al bars are illuminated by two ultrafast pump pulses ($\lambda_{\mathrm{pump}} = 400\,\mathrm{nm}$, pulse width = 150 fs, repetition rate = 76 MHz, mechanically chopped at 1 kHz) which are generated by second-harmonic generation of an ultrafast Ti:sapphire laser, and subsequently split into two pulses using a beam splitter. The pulses are focused through a microscope objective [$M = 100\mathrm{X}$, numerical aperture = 0.9, full width at half maximum (FWHM) = 3.5 μm each] onto the Al bars on either side of the nanomagnets. They cause impulsive thermal expansion, which in turn produces a periodic elastic strain along the surface that launches

*These authors contributed equally to this work.
†Corresponding author: hschmidt@soe.ucsc.edu

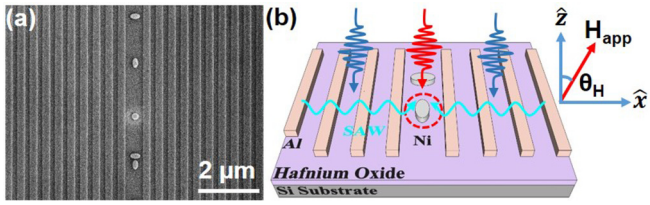

FIG. 1. (a) Scanning electron microscopy image of Ni nanomagnets embedded between an Al nanowire array. (b) Schematic plot of the SAW preferential excitation in an isolated, single elliptical Ni nanomagnet.

counterpropagating SAWs into the substrate at a velocity $\sim$3 km/s towards the Ni nanomagnet where a standing acoustic wave is formed [Fig. 1(b)]. The center of each pulse is at least 3 μm away from the nanomagnet to ensure there is negligible photoexcitation of the spin system. The magnetization dynamics are then recorded using the time-resolved magneto-optic Kerr effect (TR-MOKE) technique. A mechanically delayed probe pulse [19,22,23] (λ_{probe} = 800 nm, pulse width = 150 fs, repetition rate = 76 MHz, FWHM = 0.58 μm) is focused onto the nanomagnet and experiences a gyrotropic polarization rotation upon reflection. Lock-in detection at the pump modulation frequency is used to record the Kerr rotation (magnetic) as well as the elastic motion (nonmagnetic) using the difference and sum signal of a balanced photodetector setup. A variable external applied field (H_{app}) with an in-plane component (H_{IP}) oriented along the major axis or minor axis of elliptical Ni nanomagnets is at a fixed angle $\theta_H = 30^\circ$ from the surface normal [Fig. 1(b)].

III. RESULTS AND DISCUSSION

Figures 2(a) and 2(b) show MEL driven dynamics of the individual, orthogonally oriented nanomagnets. Here, the zero delay (Δt = 0 ns) is defined by the time it takes the acoustic wave to travel from the center of the pump illumination to the nanomagnet, which is approximately 1 ns. We observe that when the major axis of the ellipse is parallel to the acoustic wave propagation ("parallel nanomagnet") both the precession amplitude and Fourier amplitude are nearly threefold

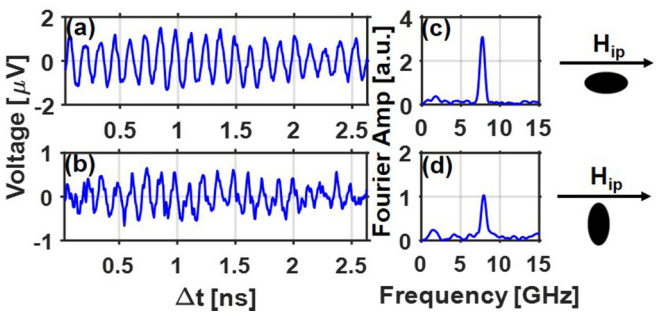

FIG. 2. (a), (b) TR-MOKE time traces at different applied fields of 2.8 and 3.2 kOe, respectively, and (c), (d) corresponding discrete Fourier-transform spectra of two resonantly excited identical, elliptical nanomagnets with orthogonal orientations. The illustrations next to panels (c) and (d) indicate the nanomagnet orientation relative to H_{IP}.

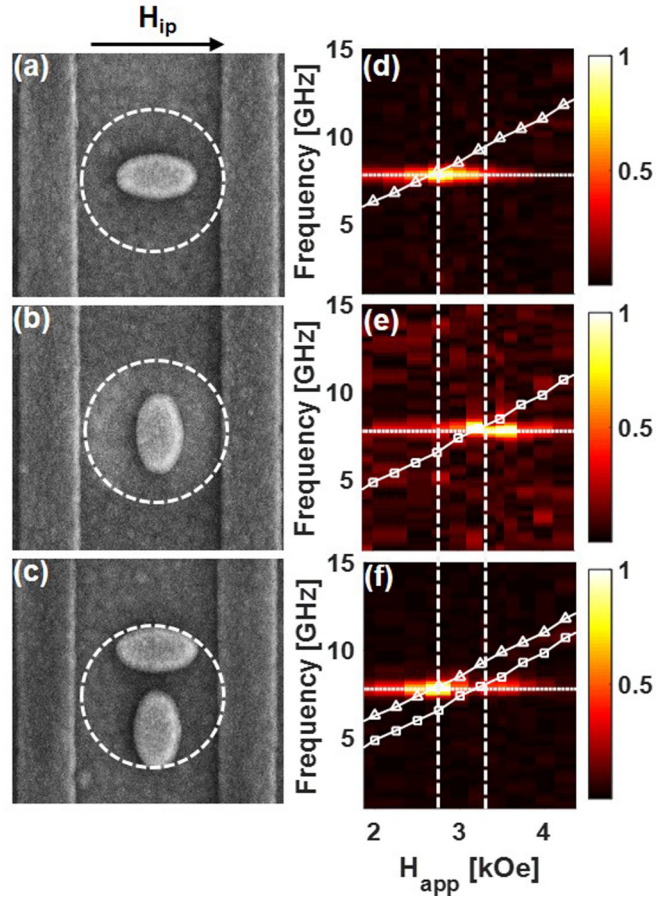

FIG. 3. (a)–(c) Scanning electron microscopy images of Ni nanomagnets embedded between Al bars and (d)–(f) corresponding field dependent Fourier spectra measurement results. The white dashed circles in panels (a)–(c) represent the position of the probe beam (FWHM = 0.58 μm). The white triangles and squares in panels (d)–(f) indicate the object-oriented micromagnetic framework simulation results when H_{IP} is along the major and the minor axis, respectively. The horizontal white dashed line is the f_{SAW} and the vertical dashed white line is a guide to the eye.

larger than the perpendicular counterpart excited at the same frequency (f_{SAW} = 7.8 GHz), as shown in Figs. 2(c) and 2(d). Furthermore, the MEL resonance for each ellipse (Fig. 3) occurs at different applied fields, H_{app} = 2.8 and 3.2 kOe for the parallel and perpendicular nanomagnets, respectively, due to the shape anisotropy. Figures 3(a)–3(c) show scanning electron microscopy images of the nanomagnets used for the field dependent measurements, which are shown in Figs. 3(d)–3(f). The oscillatory strain in the nanomagnet generates a MEL field that also oscillates at the same rate (f_{SAW}), resulting in a peak Fourier amplitude when the elastic and magnetic system are on resonance. The magnetic response is pinned to the SAW frequency over a range of applied fields, in stark contrast with the typical spin-wave dispersion obtained using conventional TR-MOKE [17,19,23]. The field dependent precession frequency for each ellipse (no applied strain) was calculated using the object-oriented micromagnetic framework and has been overlaid on the experimental colormaps in Figs. 3(d)–3(f) to verify that the MEL driven H_{res} is the

TABLE I. Summary of relevant material parameters used in the FreeFEM + + simulation of the elastic response, where E is Young's modulus, ρ is the density, α_V is the coefficient of thermal expansion, and R is the reflectivity of the material at the pump pulse wavelength $\lambda \sim 400$ nm.

Material	E (GPa)	ρ (g/cm^3)	α_V (μm/m K)	R (%)
Nickel	200	8.9	13	51
Aluminum	72	2.7	22.5	92
Hafnium oxide	161	9.68	6	14
Silicon	185	2.329	2.6	48

same applied field at which the natural magnetic frequency is identical to the SAW frequency. In Fig. 3(c), the SAW driven magnetization dynamics of the pair of nanomagnets are simultaneously probed when they are close to each other with a center-to-center distance about 310 nm. They can be clearly resolved in the field dependent Fourier spectra in Fig. 3(f). Despite the close proximity of the nanomagnets, we observe no significant change in $H_{\rm res}$ due to magnetostatic interactions between nanomagnets, which was confirmed by micromagnetic simulations [22]. These measurements unambiguously show that the SAW-driven precession of magnetic nanostructures can be selectively controlled via an externally applied magnetic field.

To supplement our experimental observations, we followed a multistep simulation procedure [16] to accurately recreate the magnetomechanical excitation. Relevant material parameters used in the simulation have been listed in Table I. In order to simulate the mechanical response, we use open-source finite-element modeling software (FreeFEM + +) to implement a two-temperature model and calculate the electron and lattice temperatures of the Al bar system in response to the impulsive photoexcitation. The simulated temperature profiles are then used to determine the thermal expansion of the periodically arranged bars, which subsequently launch SAWs into the substrate upon illumination and form a standing wave at the nanomagnet. We then use the elastic profile of the SAW-driven nanomagnet as an input into the object-oriented micromagnetic framework to calculate the induced magnetoelastic field ($H_{\rm MEL}$) [16]. The field dependent spin dynamics are converted to the frequency domain using a fast Fourier-transform algorithm and are shown in Figs. 4(a) and 4(b), which are in excellent agreement with their experimental counterparts shown in Figs. 3(e) and 3(f).

It is easy to understand that these two orthogonally oriented nanomagnets possess distinct ferromagnetic resonance modes when $H_{\rm app}$ is varied due to the shape anisotropy, thus different $H_{\rm res}$ at a given excitation frequency $f_{\rm SAW}$. However, it is also important to quantify relevant characteristics of the induced precession, i.e., MEL coupling efficiency. To characterize the dynamic response of the nanomagnetic resonators, the damping behavior of the nanomagnets is studied by analyzing the field range over which the magnetic resonance is excited as presented in Refs. [17,23]. To extract the damping parameter from the SAW-driven experiment, we consider the complex Fourier amplitude at the excitation frequency $f_{\rm SAW}$ for both simulations and experiments. The field dependence of the normalized real and imaginary parts of the discrete Fourier transform is fitted using the Lorentzian functions [23]

$$\mathrm{Im}\{F[m_z(t)]\} = \frac{1}{2\pi}\frac{\Delta H_p}{(H_{\rm app}-H_{\rm res})^2+\Delta H_p^2/2}, \quad (1)$$

$$\mathrm{Re}\{F[m_z(t)]\} = \frac{1}{\pi}\frac{16\Delta H_p(H_{\rm app}-H_{\rm res})}{4(H_{\rm app}-H_{\rm res})^2+\Delta H_p^2}, \quad (2)$$

to extract the pinning width (ΔH_p), which is directly related to the damping via the relation [23]

$$\Delta H_p = \alpha_{\rm eff}(H_{\rm app})\frac{4\pi}{\gamma}f_{\rm SAW}. \quad (3)$$

It is worth noting that we have replaced the intrinsic damping parameter in Eq. (3) with an effective damping

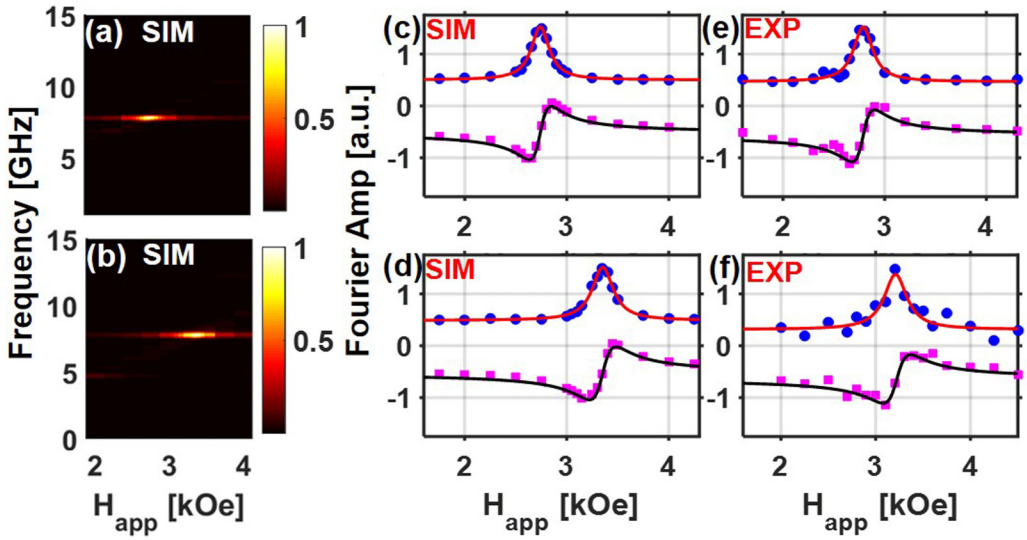

FIG. 4. (a), (b) Simulated field dependent Fourier spectra when $H_{\rm IP}$ is along the major and the minor axis, respectively, (c), (d) corresponding field dependence of the normalized complex Fourier spectra (imaginary Fourier component, circles; real Fourier component, squares) of the MEL driven dynamics, and (e), (f) corresponding experimental results.

TABLE II. Summary of the estimated pinning widths (ΔH_p) and effective damping (α_{eff}) constants for the simulated (SIM) and experimental (EXP) magnetoelastic resonances for the orthogonal ellipses, as well as the ratio between the magnetoelastic mode area and the nanomagnet surface area determined using the mode profiles shown in Figs. 5(c) and 5(d).

	ΔH_p (Oe)	α_{eff}	Mode area
Major axis // H_{IP} (SIM)	217 ± 17	0.043 ± 0.003	80%
Minor axis // H_{IP} (SIM)	244 ± 21	0.048 ± 0.004	65%
Major axis // H_{IP} (EXP)	222 ± 41	0.044 ± 0.008	
Minor axis // H_{IP} (EXP)	280 ± 109	0.055 ± 0.02	

parameter, α_{eff}, because the damping value extracted from the pinning width analysis shown in Figs. 4(e) and 4(f) of the elliptical samples is larger than the intrinsic Gilbert damping for Ni ($\alpha = 0.03$). This is contrary to our findings presented in Ref. [17] which showed that the intrinsic Gilbert damping can be determined from the SAW-driven experiment. To justify this distinction, we apply the same pinning width analysis technique to the simulated response of the ellipses shown in Figs. 4(a)–4(d). Indeed, the damping estimated from the simulated linewidth is also larger than the intrinsic Gilbert damping, which is a fixed input set to $\alpha = 0.03$ in the simulation. To verify the accuracy of the simulation, we carried out the same procedure for the cylindrical Ni nanomagnet reported in Ref. [17] ($D = 200$ nm, thickness $= 30$ nm) from which we extract a damping value of 0.034, virtually identical to the experimentally observed value. This suggests that the nanomagnet geometry is directly related to the damping behavior of the MEL-induced precession. The extracted ΔH_p and calculated α_{eff} are listed in Table II. The damping of the parallel nanomagnet is consistently smaller than that for the perpendicular ellipse for both simulation and experimental results. This finding reveals that both H_{res} and the MEL coupling efficiency depend directly on the direction of the SAW and the sample geometry.

To explain the enhanced precession amplitude for the parallel sample, we analyzed the induced MEL field, H_{MEL}, calculated in the magnetomechanical simulations and found that the maximum field amplitude is as much as threefold larger for this geometry. It is worth noting that the magnetoelastic field is not homogeneous, but varies throughout the nanomagnet due to the spatial character of the strain and magnetization. Per Ref. [22], the magnetoelastic field is calculated using the following relationships:

$$U_{\text{MEL}} = \frac{B_1}{M_s^2}\sum_i M_i^2 \varepsilon_{ii} + \frac{B_2}{M_s^2}\sum_i \sum_{j\neq i} M_i M_j \varepsilon_{ij}, \quad (4)$$

$$H_{\text{MEL}} = -\frac{\delta U_{\text{MEL}}}{\delta \vec{M}}, \quad (5)$$

where B_1 and B_2 are the magnetoelastic constants (7.85×10^7 erg/cm for Ni) and ε is the three-dimensional strain tensor. Thus, per Eqs. (4) and (5), H_{MEL} depends on both the magnetic orientation and the induced strain profile. From the micromagnetic simulations, we observe that the magnetization vectors of both samples lie in the x-z plane and are slightly misaligned with the applied field. For the parallel and perpendicular samples, the polar angles (θ_M) of their magnetic vectors ($\vec{M}$) with respect to surface normal are 51.5° and 46.4°, respectively. Therefore, the differences between the induced magnetoelastic fields are primarily due to the distinct strain profiles of each sample. We now turn our attention to the ferromagnetic resonance mode profiles of the nanomagnets [Figs. 5(a)–5(d)] excited by both a small, field-like pulse ("natural response") and by acoustic waves ("forced response"). Here, the "natural response" refers to the intrinsic spin dynamics when the nanomagnets are not driven at the SAW frequency and it simply follows from the Landau-Lifshitz-Gilbert equation. For the samples studied here, we observe a single, well-defined mode over an extended field range. Thus, the natural response profiles shown in Figs. 5(a) and 5(b) are simply the Fourier spectra of the impulsively excited nanomagnets under identical applied fields as their elastically driven counterparts. Now, we compare the natural and forced responses and find that the profile of the SAW-driven excitation is much closer to the natural response for the parallel sample, which is consistent with the higher-quality resonance we have observed in the measurement. To quantitatively compare the mode distributions, we determined the area of the nanomagnets with at least 63% of the maximum Fourier amplitude (at f_{SAW}) and divided it by the total area of the nanomagnet ($\sim 0.04\,\mu\text{m}^2$). This calculation reveals an approximately 15% difference in the mode homogeneity of the two identical nanomagnets, which suggests that the mode homogeneity inside the nanomagnet also may play an important role on the damping. The remarkable agreement

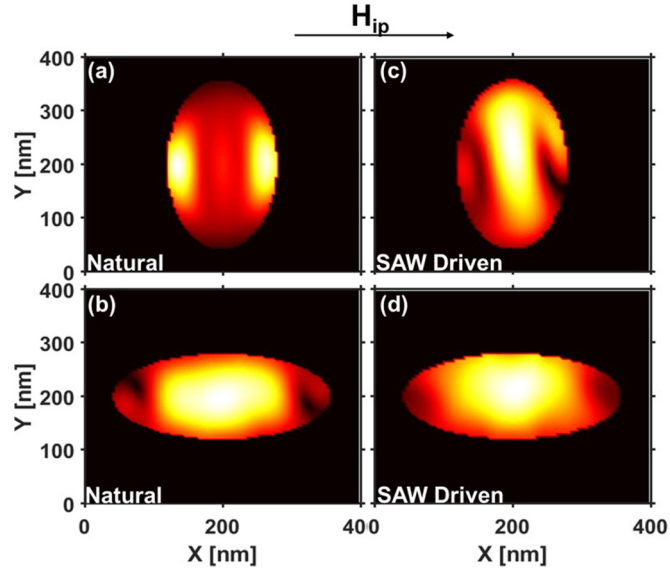

FIG. 5. Simulated mode profiles ($f = 7.8$ GHz) for the (a) perpendicular ($H_{\text{app}} = 3.2$ kOe) and (b) parallel nanomagnets ($H_{\text{app}} = 2.8$ kOe) excited by a small field pulse (no SAWs). We note again that no higher-order spin waves are present in the samples studied here. In panel (c), the profile of the SAW-driven, perpendicular nanomagnet shows that the mode has been forced to the center of the nanomagnet, while in panel (d) we see that the mode profile of the SAW-driven, parallel nanomagnet is much closer to the natural response in panel (b).

between experiment and simulations supports the notion that the efficiency, or quality, of the MEL excitation can be directly controlled via the sample geometry. We have shown that this approach is most effective when the acoustic wave travels along the easy axis of the nanomagnet, which is determined by the shape anisotropy in our case. Further studies involving strong magnetocrystalline anisotropies may provide yet another degree of freedom that may be used to tune the response of the device.

IV. CONCLUSION

In conclusion, we used optically generated SAWs as a source of "cold" excitation to selectively trigger spin dynamics in magnetic nanostructures via MEL coupling. Using two identical, elliptical nanomagnets with orthogonal orientations, we showed that the shape anisotropy can be exploited to preferentially excite one of the nanomagnets by controlling the applied field. In addition, analysis of the damping behavior showed that the MEL coupling efficiency for these two nanomagnets depends on the direction of the SAW and sample geometry. These findings are in excellent agreement with micromagnetic simulations and may provide important reference for the design and application of nanoscale magnetomechanical devices.

ACKNOWLEDGMENTS

We acknowledge T. Yuzvinsky and the W. M. Keck Center for Nanoscale Optofluidics at University of California Santa Cruz. This work was supported by the National Science Foundation under Grants No. ECCS-1509020 and No. DMR-1506104 and the Samsung Global MRAM Innovation program by Samsung, Inc.

[1] B. Behin-Aein, D. Datta, S. Salahuddin, and S. Datta, Nat. Nanotechnol. **5**, 266 (2010).
[2] A. Kikitsu, J. Magn. Magn. Mater. **321**, 526 (2009).
[3] M. K. Grobis, O. Hellwig, T. Hauet, E. Dobisz, and T. R. Albrecht, IEEE Trans. Magn. **47**, 6 (2011).
[4] T. R. Albrecht, H. Arora, V. Ayanoor-vitikkate, J.-M. Beaujour, D. Bedau, D. Berman, A. L. Bogdanov, Y.-A. Chapuis, J. Cushen, E. E. Dobisz, G. Doerk, H. Gao, M. Grobis, B. Gurney, W. Hanson, O. Hellwig, T. Hirano, P.-O. Jubert, D. Kercher, J. Lille, Z. Liu, C. M. Mate, Y. Obukhov, K. C. Patel, K. Rubin, R. Ruiz, M. Schabes, L. Wan, D. Weller, T.-W. Wu, and E. Yang, IEEE Trans. Magn. **51**, 0800342 (2015).
[5] J. Torrejon, M. Riou, F. A. Araujo, S. Tsunegi, G. Khalsa, D. Querlioz, P. Bortolotti, V. Cros, K. Yakushiji, A. Fukushima, H. Kubota, S. Yuasa, M. D. Stiles, and J. Grollier, Nature (London) **547**, 428 (2017).
[6] S. Tsunegi, T. Taniguchi, R. Lebrun, K. Yakushiji, V. Cros, J. Grollier, A. Fukushima, S. Yuasa, and H. Kubota, Sci. Rep. **8**, 13475 (2018).
[7] T. Taniguchi and H. Kubota, Jpn. J. Appl. Phys. **57**, 053001 (2018).
[8] J. Walowski and M. Münzenberg, J. Appl. Phys. **120**, 140901 (2016).
[9] S. Baierl, M. Hohenleutner, T. Kampfrath, A. K. Zvezdin, A. V. Kimel, R. Huber, and R. V. Mikhaylovskiy, Nat. Photonics **10**, 715 (2016).
[10] J. C. Slonczewski, J. Magn. Magn. Mater. **159**, L1 (1996).
[11] A. V. Kimel, A. Kirilyuk, P. A. Usachev, R. V. Pisarev, A. M. Balbashov, and T. Rasing, Nature (London) **435**, 655 (2005).
[12] E. Beaurepaire, J. C. Merle, A. Daunois, and J. Y. Bigot, Phys. Rev. Lett. **76**, 4250 (1996).
[13] S. Davis, A. Baruth, and S. Adenwalla, Appl. Phys. Lett. **97**, 232507 (2010).
[14] M. Foerster, F. Macià, N. Statuto, S. Finizio, A. Hernández-Mínguez, S. Lendínez, P. V. Santos, J. Fontcuberta, J. M. Hernàndez, M. Kläui, and L. Aballe, Nat. Commun. **8**, 407 (2017).
[15] M. Weiler, H. Huebl, F. S. Goerg, F. D. Czeschka, R. Gross, and S. T. B. Goennenwein, Phys. Rev. Lett. **108**, 176601 (2012).
[16] Y. Yahagi, B. Harteneck, S. Cabrini, and H. Schmidt, Proc. SPIE **9371**, 93711O (2015).
[17] W. G. Yang, M. Jaris, D. L. Hibbard-Lubow, C. Berk, and H. Schmidt, Phys. Rev. B **97**, 224410 (2018).
[18] S. Mondal, M. A. Abeed, K. Dutta, A. De, S. Sahoo, A. Barman, and S. Bandyopadhyay, ACS Appl. Mater. Interfaces **10**, 43970 (2018).
[19] Y. Yahagi, B. Harteneck, S. Cabrini, and H. Schmidt, Phys. Rev. B **90**, 140405(R) (2014).
[20] S. Wang, A. Barman, H. Schmidt, J. D. Maas, A. R. Hawkins, S. Kwon, B. Harteneck, S. Cabrini, and J. Bokor, Appl. Phys. Lett. **90**, 252504 (2007).
[21] N. Qureshi, S. Wang, M. A. Lowther, A. R. Hawkins, S. Kwon, A. Liddle, J. Bokor, and H. Schmidt, Nano Lett. **5**, 1413 (2005).
[22] Y. Yahagi, C. R. Berk, B. D. Harteneck, S. D. Cabrini, and H. Schmidt, Appl. Phys. Lett. **104**, 162406 (2014).
[23] Y. Yahagi, C. Berk, B. Hebler, S. Dhuey, S. Cabrini, M. Albrecht, and H. Schmidt, J. Phys. D **50**, 17LT01 (2017).